Dynamics of Cu-Zr metallic glass devitrification under ultrafast laser excitation revealed by atomistic modeling

Djafar Iabbaden, Jonathan Amodeo, Claudio Fusco, Florence Garrelie, Jean-Philippe Colombier

Dynamics of Cu-Zr metallic glass devitrification under ultrafast laser excitation revealed by atomistic modeling

Djafar Iabbaden,[1,*] Jonathan Amodeo,[2] Claudio Fusco,[3] Florence Garrelie,[1] and Jean-Philippe Colombier[1,†]

[1] *Univ Lyon, UJM-Saint-Etienne, CNRS, IOGS, Laboratoire Hubert Curien UMR5516, F-42023 St-Etienne, France*
[2] *Aix Marseille Univ, Université de Toulon, CNRS, IM2NP, Marseille, France*
[3] *Univ Lyon, INSA Lyon, CNRS, MATEIS, UMR 5510, F-69621 Villeurbanne, France*

(Dated: November 14, 2023)

The physics of metallic glass local devitrification employing ultrafast laser irradiation is the cradle of complex phenomena that are still not understood despite its applicative potential in material processing for nanotechnology. This paper reports a theoretical simulation combining the two temperature model and classical molecular dynamics simulations to unravel the mechanisms that lead to the localized phase transition in Cu-Zr metallic glass. According to observations, the initial composition of amorphous samples plays an essential role, in addition to nonequilibrium thermodynamic processes caused by the laser energy deposition that alters the atomic environment. We further demonstrate that specific compositions devitrify despite its high glass-forming ability. The thermodynamic conditions fostering the emergence of a stable nanocrystalline phase are clearly established. The compressive pressure wave and the rapid heating process caused by ultrafast laser energy deposition synergistically contribute to disrupt the microstructure of the glass significantly, thereby initiating the devitrification process. Results are discussed using additional classical MD simulations that provide valuable insights for interpreting the distinct contributions of temperature and pressure to the phase transformation. Finally, the impact of the formed nanocrystals on the phononic thermal conductivity of the alloy is presented confirming the potential application of the laser-induced devitrification process for the development of a new generation of nanoarchitectured materials.

I. INTRODUCTION

Ultrafast laser processes causing structural modification in ordered nanocrystalline alloys or metastable systems such as metallic glasses (MGs) have been extensively investigated in experimental and theoretical studies [1]. Several applications were the object of a particular focus because of their attractive properties, including magnetic fabrication [2], electrocatalysis for energy storage [3], coatings properties [4], standing ductility [5], catalysis [6], and optical applications [7]. The fact remains that all these efforts to design a material with exceptional properties are still far from fulfilling all fabrication challenges. One of the approach is to create nanocomposite alloys combining crystalline and amorphous structures [8]. These hybrid materials may inherit properties from either the amorphous or nanocrystalline phases, or even exhibit unexpected outstanding properties due to anisotropic characteristics induced by the presence of nanocrystals within the amorphous material [9–13]. Conventional annealing method is the most popular technique proposed in the literature to achieve devitrification. This consists in maintaining the amorphous sample long enough in a temperature region below the melting temperature and above its glass transition temperature to crystallize [14–16]. The main drawbacks of this approach are the spontaneous aspect and the uncontrolled spatial character of the devitrification in MGs [17]. New strategies to control the final crystalline phase, the rate of seeds emergence, their location and size are required. In general, this disorder-order transformation depends on the Glass-Forming Ability (GFA) of the material, which translates to its ability to form an amorphous structure [18]. In this context, the ultrafast laser seems to be one the most appropriate tool to overcome this limitation.

Monoatomic metallic structures are difficult to amorphize and tend to remain crystalline due to their low GFA [19, 20]. Experimental and theoretical vitrification processes in liquid metals during rapid quenching confirm this behavior, as demonstrated in Al, Ti, Fe, Ni, and Cu [21–28]. Nevertheless, a novel experimental method known as ultrafast quenching technique with an ultrahigh cooling rate was developed to achieve the amorphization of pure metallic elements Ta and V [29]. Furthermore, numerous studies have shown that binary alloys have the potential to undergo amorphous-crystal phase transition over a wide range, such as NiZr [30–33], CuTi [34, 35], PdSi [36], FeNi [37, 38], SiAl [39, 40], SiAu [41], NiAu [42], and NiAl [43]. The study on NiNb MG highlights that from a thermodynamics point of view, the maximum devitrification occurs around the glass transition temperature (T_g) [44, 45]. Recent work on ZrCo MG provides another pathway to understand the devitrification mechanism, where atomic species and concentration play an important role (Co concentration in the range of 30-90 %) [46]. Devitrification process is even sought for multicomponent MG mixtures. As reported in the literature, it concerns ternary alloys such as CuZrPd [47], AlNiCo [48], CuZrAl [49, 50], and

* djafar.iabbaden@univ-st-etienne.fr
† jean.philippe.colombier@univ-st-etienne.fr

Published in Acta Materialia in November 2023, please cite as: Iabbaden, D., Amodeo, J., Fusco, C., Garrelie, F., & Colombier, J. P. (2023). Dynamics of Cu-Zr metallic glass devitrification under ultrafast laser excitation revealed by atomistic modeling. Acta Materialia, 119487.

AlNiLa [51]. Several studies have achieved devitrification in multicomponent amorphous systems in supercooling condition, namely ZrCoAlFe [52], LaAlNiCu [53], ZrTiNiCuBe [54, 55], and ZrTiCuNiAl [56]. The authors support that the atomic element size and the stoichiometry of mixtures are fundamental ingredients to realize devitrification.

Due to the high GFA of some alloys, devitrification can be challenging. This was confirmed by comparing the nucleation rates of two amorphous alloys using a crystal/liquid interfacial setup. The work highlights a significantly slower crystal growth rate for CuZr compared to low-GFA NiAl [57]. To reduce the large GFA of CuZr MG, different methods were proposed with the aim of activating devitrification. We can mention the sandwiching method that consists in confining CuZr MG between two pure Zr and Cu layers that allows the emergence of nanocrystals [58]. The work [59] relies on a seeding method where a BCC crystalline structure is inserted within the amorphous material to trigger devitrification. Furthermore, the devitrification of CuZr MG using X-ray was confirmed experimentally, but no mechanism was proposed for such a process [60]. In laser processing, ultrafast laser irradiation can be used to induce the amorphous-crystal transformation [61]. However, the mechanism and thermodynamic conditions behind this transformation remain largely unknown [62–71]. An attempt was made to study ultrafast laser interactions with amorphous CuZr targets using atomistic computations but no successful transition from amorphous to crystalline structure was reported [72].

In the physical vapor deposition (PVD) process, MG thin films are engineered with specific properties that differ from the substrate that can be designed for specific optical, thermal and mechanical applications. Laser irradiation has the significant advantage of being able to process the film without affecting the substrate [73, 74]. This versatility enables MG devitrification and thus the creation of a composite at a specific location using a single-step treatment, rather than multiple steps or processes making this experimental method highly adaptable. Ideal laser conditions remain hard to reach while the elementary physical processes responsible for the laser-matter reaction are still ambiguous. Our study relies on a theoretical approach that combines a two temperature model (TTM) and classical molecular dynamics (MD) simulations used to investigate laser conditions and CuZr composition as well as to analyze the devitrification mechanisms at the surface of thick irradiated samples. First, several CuZr compositions are tested to identify stable MG to be subjected to the laser treatment. Then, the impact of the laser on the sample is investigated in terms of pressure waves propagation and temperature as well as local atomic rearrangements with the aim of justifying the occurrence of nanocrystals within the glassy matrix. Results are discussed in the light of additional classical MD simulations following relevant thermomechanical paths. The study concludes with a discussion about thermal conductivity calculations performed on the nanostructured MG.

II. COMPUTATIONAL DETAILS

The laser-material interaction process in amorphous (α) CuZr alloys is modelled using a TTM-MD hybrid method [75–79] as implemented in the LAMMPS software [80, 81]. Several initial random solid solutions with BCC-like crystalline structure and various stoichiometry including $Cu_{19.4}Zr_{80.6}$, $Cu_{19.9}Zr_{80.1}$, $Cu_{21.9}Zr_{78.1}$, $Cu_{23.5}Zr_{76.5}$, $Cu_{24.9}Zr_{75.1}$, and $Cu_{26}Zr_{74}$ were first modeled using the embedded atom model parameterization of Mendelev *et al* [82]. Each 3D-periodic $8.13 \times 8.13 \times 8.13$ nm^3 simulation cell is filled with 31250 atoms and is subjected to a classical amorphization cycle using MD as described in Ref. [83]. First, the system is heated up to 2000 K in the liquid state at a rate of 10^{13} K.s^{-1} and then it is quenched down to 300 K using a rate of 10^{11} K.s^{-1} where another equilibration run is performed during 100 ps in the NPT ensemble (isothermal-isobaric) using the Nosé-Hoover thermostat and barostat [84]. An MD timestep of δt=1 fs is used for all simulations. Then the obtained amorphous cell is replicated in the three direction of space to extend the sample size, following the classical procedure of Cao *et al* [85]. Finally, the simulation box is extended twice (vacuum region) in the X-direction to create the surface of the material and is further equilibrated for another 100 ps.

The TTM-MD equations are solved on an electronic grid of $702 \times 1 \times 1$ during 30 ps. Ultrafast laser operating conditions of pulse duration τ=100 fs and absorbed fluence F_{abs}=34 mJ/cm^2 are employed to preclude the system from ablation. After the laser pulse, the system is tracked during 16 ns without thermomechanical constrains. To effectively prevent pressure wave reflection at the rear surface of the bulk sample, a damping region known as the Non-Reflecting Boundary Condition (NRBC) is employed, as outlined in Ref [83]. This region is characterized by a damping coefficient γ_{damp}=2.5 10^{-3} eV ps Å^{-2}. The TTM solver incorporates electronic properties, as documented in Ref. [83], which compiles data from multiple sources, including Refs. [72, 83, 86, 87]. It is assumed that these electronic properties exhibit minimal variation with changes in composition within amorphous CuZr alloys. All the structural analysis are performed using the Common Neighbor Analysis (CNA) [88] and Polyhedral Template Matching (PTM) [89] algorithms as implemented in the OVITO software [90] applied here to Cu and Zr sublattices.

III. RESULTS AND DISCUSSION

A. CuZr amorphous configurations

Considering the high GFA of CuZr systems in the range 30≤%-Zr≤50 [91], the strategy is to build a stable Zr-rich amorphous structure to boost the probability to activate devitrification. For this purpose, six structures with different compositions are tested. The final results are illustrated in Figure 1 where the CNA algorithm is used without chemistry considerations.

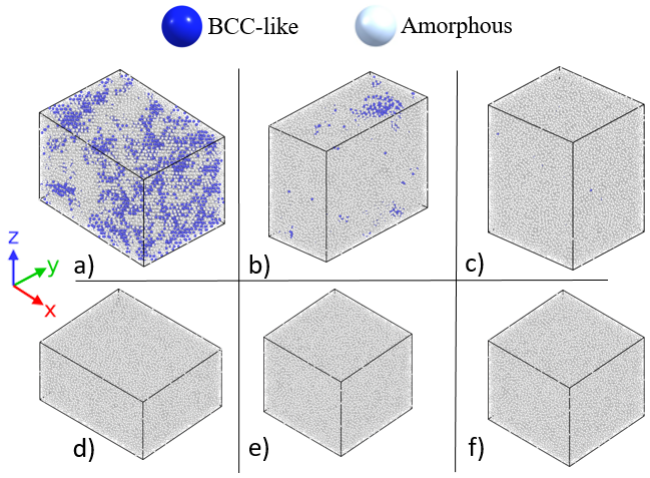

Figure 1. $Cu_{1-x}Zr_x$ MG samples produced after the amorphization cycle. The compositions are: a) $Cu_{19.4}Zr_{80.6}$, b) $Cu_{19.9}Zr_{80.1}$, c) $Cu_{21.9}Zr_{78.1}$, d) $Cu_{23.5}Zr_{76.5}$, e) $Cu_{24.9}Zr_{75.1}$, and f) $Cu_{26}Zr_{74}$. The local atomic structure is characterized using CNA (blue=BCC-like configurations, grey=amorphous).

Figure 1 presents the local structures analysis obtained for the various stochiometries after the amorphization process. The different compositions exhibit a competition between the amorphous and crystalline phases. Three contrasted behaviors are observed. Firstly, in Figure 1 a), the α-$Cu_{19.4}Zr_{80.6}$ partially crystallizes during the process with ∼40 % of the atoms characterized by a BCC-like structure. Secondly, in Figure 1 b), the α-$Cu_{19.9}Zr_{80.1}$ is also partially crystallized with BCC-like clusters corresponding to 4 % of the total amount of atoms. Finally, the last samples are completely stabilized MGs as illustrated in Figure 1 c), d), e) and f) corresponding to α-$Cu_{21.9}Zr_{78.1}$, α-$Cu_{23.5}Zr_{76.5}$, α-$Cu_{24.9}Zr_{75.1}$ and α-$Cu_{26}Zr_{74}$, respectively. A complementary analysis based on Radial Distribution Function (RDFs) is shown in Figure 2.

The results reveal that for the completely vitrified amorphous structures α-$Cu_{26}Zr_{74}$, α-$Cu_{24.9}Zr_{75.1}$, α-$Cu_{23.5}Zr_{76.5}$ and α-$Cu_{21.9}Zr_{78.1}$ a double splitting of the RDFs second peak typical of amorphization is noticed whatever the stoichiometry. On the contrary, a single pronounced peak is observed for the α-$Cu_{19.4}Zr_{80.6}$ structure which is the footprint of an already existing crystal.

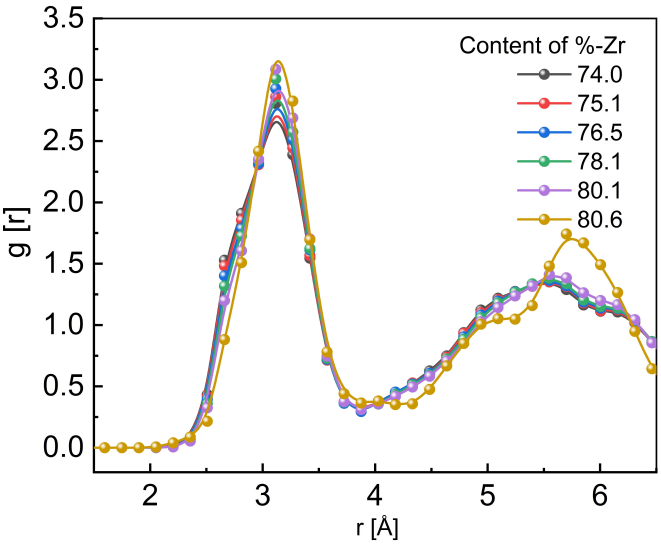

Figure 2. RDFs of the various CuZr MGs after the amorphization process. The complete amorphization of the sample is characterized by the double splitting of the second peak.

An additional simulation is performed on the α-$Cu_{21.9}Zr_{78.1}$ sample to verify that the structure is stable and does not undergo spontaneous crystallization. The sample is subjected to an additional equilibration simulation of 100 ns in the NPT ensemble at 300 K and 1 bar using the Nosé-Hoover thermostat and barostat. The results confirm the metastable character of the glass where no crystal is detected (see supplementary materials). In the following, the amorphous α-$Cu_{21.9}Zr_{78.1}$ is selected as the initial structure to investigate the devitrification process triggered by ultrafast laser irradiation. This amorphous cell is replicated up to 211.31 × 7.61 × 10.50 nm^3 size.

B. Ultrafast laser irradiation of α-$Cu_{21.9}Zr_{78.1}$

Figure 3 shows a specific region within the α-$Cu_{21.9}Zr_{78.1}$ at t∼8 ns after the laser energy deposition. The CNA algorithm recognizes the emergence of BCC-like crystalline germs within the amorphous matrix. This structure matches the prediction of the CuZr phase diagram at high-temperature where a solid solution of Cu in the BCC β-Zr phase is expected for this specific composition [92]. The characteristic size of the crystalline nanocrystals that nucleate in the subsurface region is lower than 1 nm. The growth of the crystalline phase deeper inside the material is shown in Figure 4.

Figure 4(a) indicates that the first crystal seeds within the $Cu_{21.9}Zr_{78.1}$ amorphous structure do not form instantly after the laser pulse but at t∼8 ns in a region located at X∼63 nm. As the seeds grow, they coalesce to form a crystallization front at t=9 ns and

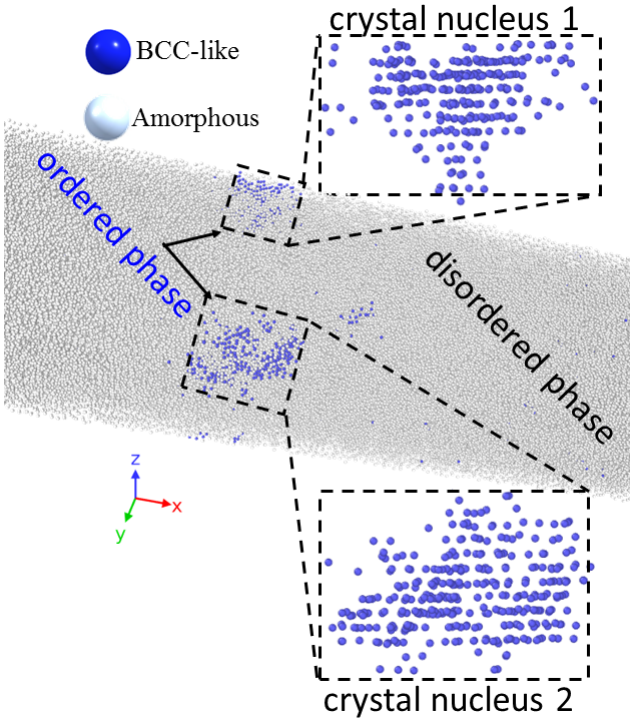

Figure 3. Nucleation of BCC-like nuclei (∼15 atomic plans) within the amorphous α-$Cu_{21.9}Zr_{78.1}$ at t∼8 ns after the laser-energy deposition.

travel through the devitrified region that reaches a final thickness of ∼30 nm at the end of the process. The freshly nucleated crystal phase is not transient and survives until the end of the simulation at t=16 ns. Furthermore, Figure 4(b) emphasizes the devitrified region at t=16 ns where the PTM analysis clearly shows crystallographic planes. The CuZr nanocrystals have the global Cu (21.9 %) and Zr (78.1 %) concentrations without segregation/crystallization effects. A detailed analysis was performed to identify the number of BCC-like atoms and the propagation velocity of the crystal front. The results are shown in Figure 5.

Figure 5 provides the variation of the crystallization front relative position ΔX=$X(t)$-$X(0)$ with $X(0)$=63 nm as function of time. At t=9 ns, the fraction of crystalline phase is originally ∼5 %. Beyond t=9 ns, the crystallization front travels the sample which permits the crystalline phase fraction to increase up to 55 % at t=16 ns. The front propagates toward the melted surface (-X direction) with an average velocity of 2.77 m.s^{-1} (∼100 times slower than the sound velocity in air). This means that the crystallization is partial, localized (∼0-30 nm) and relatively slow as compared *e.g.,* to the devitrification of CuTi amorphous alloys that occurs only under supercooling condition with a crystallization front velocity of ∼40 m.s^{-1} [35].

To track the emergence of crystalline solid solution during devitrification, a complementary analysis involving RDFs at several key times is computed in the devitrified region (35≤X≤63 nm), see Figure 6. At t=0 ns, we observe that the structure is amorphous, characterized by the presence of the second peak double splitting. At t=5 ns, the decrease of the first peak intensity together with the disappearance of the double splitting and the appearance of a broader second peak indicate that the system liquefies in this region. Beyond t=5 ns, the intensity of the first peak starts to increase and the shape of RDFs becomes sharper confirming a local ordered atomic rearrangements. The first and second peaks reach their maximum at t=16 ns where no double peak is observed. Instead, a single narrowed peak that indicates the growth of a crystalline structure within the amorphous material is detected.

C. Origins of the devitrification process

When the laser energy is delivered, the system is driven to a nonequilibrium state where electrons are hot and the lattice is still relatively cold. Therefore, a process of electron-phonon relaxation takes place to balance the energy. The two temperature dynamics defines an ionic temperature gradient inducing stress accumulation that manifests in the form of a compression pressure wave followed by a rarefaction pressure wave due to relaxation of the system. Pressure waves operate at times between t=0-200 ps. The computed spatial evolution of pressure is shown in Figure 7.

At t=5 ps, the pressure reaches its maximum value of ∼4 GPa and gradually dwindles to ∼3.1, 2.2, 1.7, 0.2 GPa associated to t=15, 20, 30, and 200 ps respectively. Moreover, a negative pressure of ∼−1 GPa corresponding to the rarefaction pressure wave propagation is detected at t=80-100 ps. As mentioned previously, the amorphous-crystal transformation starts at t∼8 ns, much later after the complete absorbance of the pressure waves.

To interpret the devitrification phenomenon, in the following we further investigate the local atomic rearrangements evolution of the sample during the process. All MG exhibit a unique fraction of polyhedra atomic configurations, which is considered as the footprint of the amorphous structure. In this context, it is generally argued that the formation/breakage of the polyhedra network has a major impact on the glass phase stability [93]. Here, we track the proportions of the two most prevalent polyhedra, namely <0, 1, 10, 4> ($Z15_{I1}$) and <0, 2, 8, 5> ($Z15_{I2}$), in the devitrified region as well as in a non-devitrified domain. The polyhedra fraction evolution is shown in Figure 8.

At t=0 ns, Figure 8 shows a significant fraction of polyhedra in the initial structure *c.a.,* 2.4 and 4.2 % in both regions for $Z15_{I1}$ and $Z15_{I2}$, respectively. However, these fractions quickly drop down to 1.1, and 2.1 % at

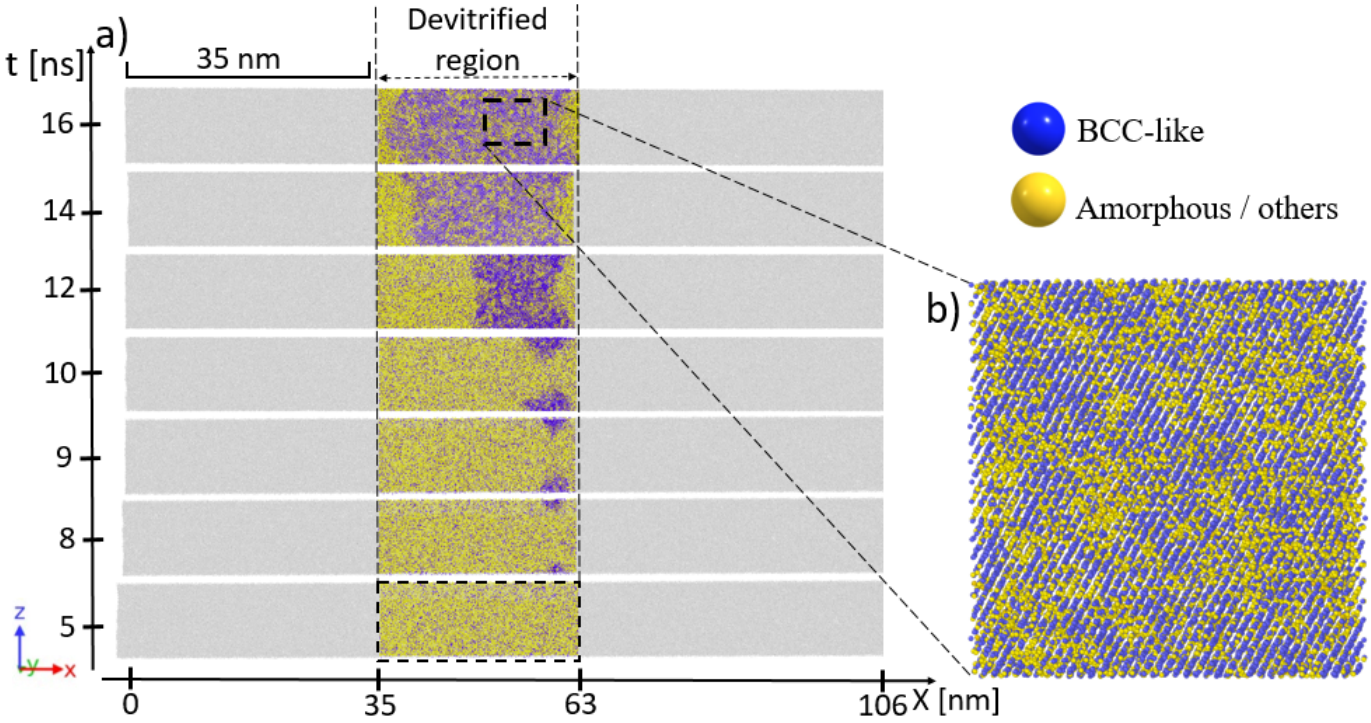

Figure 4. α-$Cu_{21.9}Zr_{78.1}$ atomic configurations after ultrafast laser irradiation as a function of time. Emphasize of the devitrified region: a) global view of the devitrified region located at $35 \leq X \leq 63$ nm, b) magnification of a devitrified subdomain at t=16 ns. The atoms are colored according to their local atomic structure computed using the PTM algorithm. Atoms colored in grey rely to hidden amorphous and liquid domains.

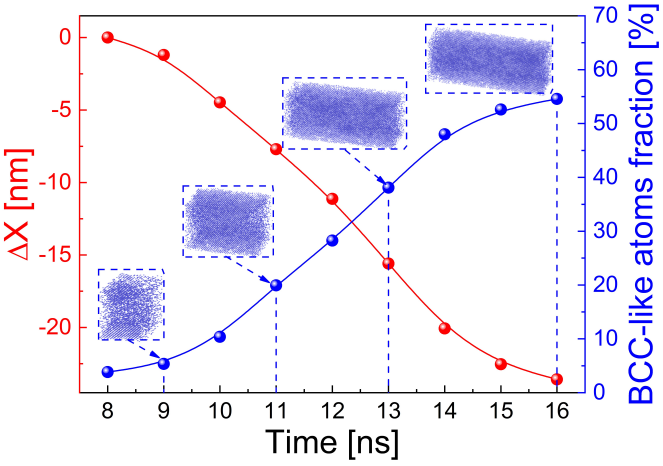

Figure 5. Mean position of the crystallization front's propagation toward the surface versus time at t=8-16 ns during the devitrification process in the α-$Cu_{21.9}Zr_{78.1}$ MG sample. In blue, we can notice the formed crystalline BCC-like atoms at t=9, 11, 13 and 16 ns.

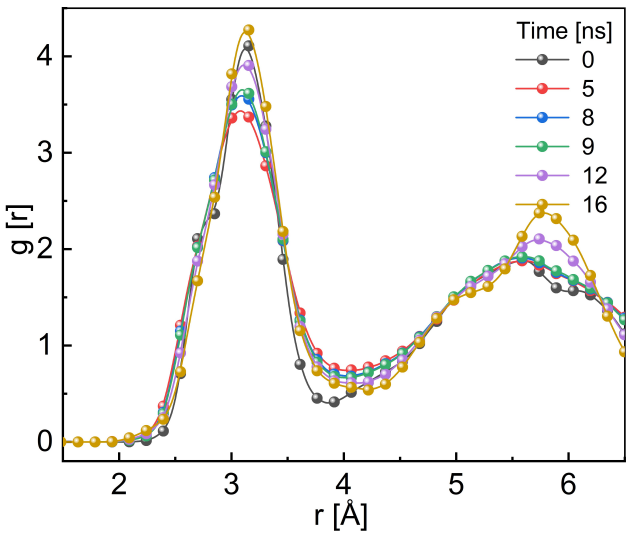

Figure 6. RDFs evolution in the α-$Cu_{21.9}Zr_{78.1}$ sample at different times during the devitrification process. The double splitting of the secondary peak typical of the amorphous state disappears proving the emergence of a crystalline structure.

t=0.05 ns in the region that will devitrify. No significant variation of the polyhedra fraction was noticed in the non-devitrified region. The insets in both Figure 8(a) and (b) show that a significant reduction in the fraction of polyhedra within the devitrified region occurs

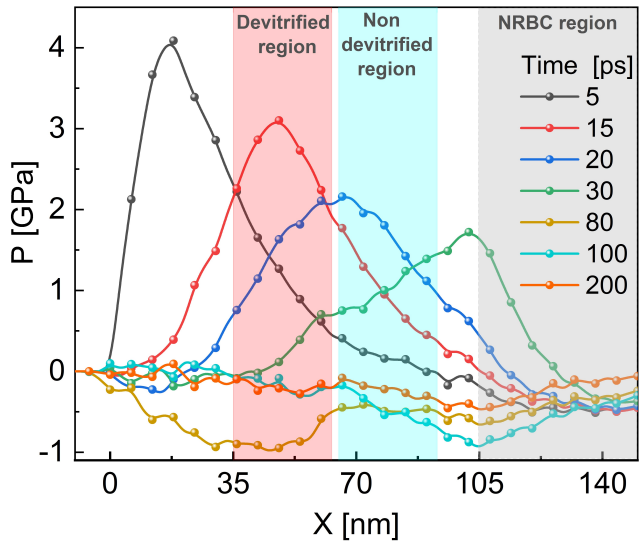

Figure 7. Spatial evolution of the local pressure profile in α-$Cu_{21.9}Zr_{78.1}$ at t=0-200 ps. The laser processing conditions are τ=100 fs, F_{abs}=34 mJ/cm^2 for the pulse duration and absorbed fluence respectively. A devitrified zone (in salmon), a non-devitrified zone (in aqua) are chosen to compare the impact of pressure on polyhedra, and NRBC region (in gray).

primarily within t=0-0.05 ns. This time interval aligns with the period during which both the compression wave and the temperature peak progress, as depicted in Figures 7 and 9, respectively. On contrary, the rarefaction wave has the same maximum amplitude of $\sim$−1 GPa within both the devitrified and non-devitrified investigated regions. Furthermore, it is worthy to notice that while the pressure quickly vanishes after t=0.2 ns, the polyhedra breaking process stops and a steady-state regime sets in with a proportion of 0.9 % $Z15_{I1}$ and 1.9 % of $Z15_{I2}$ until $\sim$5 ns in the devitrified region. An intermediate regime, associated with the frustration and recombination of polyhedra is recorded within the devitrified region at $t\sim$5-8 ns time range whereas the non-devitrified region is found to have a constant proportion of $Z15_{I1}$ and $Z15_{I2}$ polyhedra equivalent to those observed before the laser energy deposition. When the system devitrifies at $t>$8 ns, the fraction of both $Z15_{I1}$ and $Z15_{I2}$ decreases to 0.3 and 0.7 % in the devitrified region, respectively.

Investigating more carefully the time-evolution of the temperature profile (Figure 9), we notice at t=5 ps the amorphous-liquid transition in the $X<$40 nm region with a maximum temperature $T\sim$3000 K ($T_m\approx$1440 K). Moreover, the temperature drops from $\sim$1800 to 1250 K in the devitrified region for $1\leq t\leq$8 ns marking a thermal relaxation of the amorphous sample. At t=8 ns, $T\sim$0.87 T_m and this corresponds to the time where the first crystal seed is formed as shown in Figure 3. The temperature gradually decreases to $T\sim$780 K slightly below the theoretical temperature $T_g\sim$830 K.

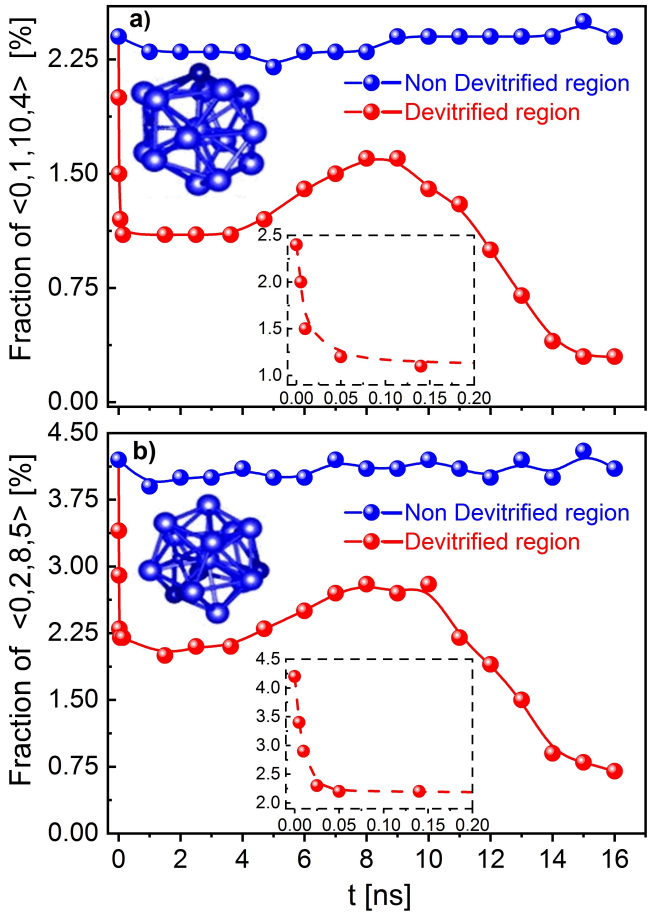

Figure 8. Time evolution of the polyhedra at t=0-16 ns within the α-$Cu_{21.9}Zr_{78.1}$ MG in the devitrified region located at $35\leq X\leq 63$ nm and in a non-devitrified domain located at $65\leq X\leq 93$ nm, a) <0, 1, 10, 4>, b) <0, 2, 8, 5>. A zoom in the time range of 0-0.2 ns is provided.

At t=16 ns, the amount of crystalline structure becomes relatively stable, and the crystallization wave ceases to propagate. As a consequence, we conclude that the fast cooling stage from T_m to T_g is a determinant mechanism to promote the devitrification process in a region where the local atomic skeleton made of the $Z15_{I1}$ and $Z15_{I2}$ polyhedra has already undergone significant disorganization. In addition, it is noteworthy that the temperature in the non-devitrified zone is below T_g. This confirms that the optimal temperature range to favor crystal nucleation is in the vicinity of T_g. This thermodynamics kinetic tendency is fostered by the sharp increase of the viscosity below T_g that prevents any substantial atoms reorganization.

In the following, a computation is performed to determine the critical temperature T_c below which the crystals are formed and compare it to the previous temperature determined at 8 ns ($\sim$0.87 T_m). An additional brick of comprehension is brought by invoking classical nucle-

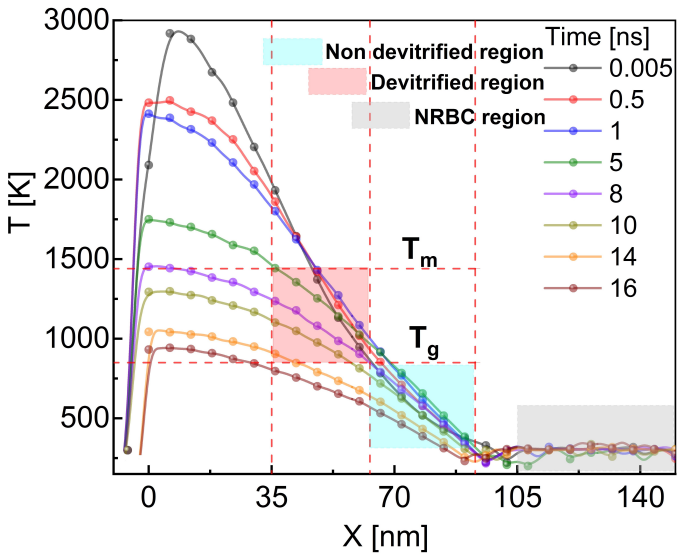

Figure 9. Spatial evolution profile of the local lattice temperature in α-$Cu_{21.9}Zr_{78.1}$ at several key times 0.005, 0.5, 1, 5, 8, 10, 14, and 16 ns of the devitrification process. A devitrified zone (in salmon) and a non-devitrified zone (in aqua) are chosen to investigate the impact of temperature on the devitrification process.

ation models [94, 95]. The standard Classical Nucleation Theory (CNT) assumes that devitrification occurs in two correlated distinct stages namely nucleation and growth. The devitrification that intervenes in α-$Zr_{78.1}Cu_{21.9}$ is homogeneous, in contrast to the heterogeneous process that may intervene due to impurities or crystalline seeds already present in the amorphous structure.

As shown in Figure 3, the nucleation starts with the emergence of a nucleus with a minimal critical size ($\sim$2$-$5 Å) that settles within the amorphous matrix [96]. Assuming that the formed nucleus has a spherical shape, the change of Gibbs free energy in an undercooled liquid is defined by Equation 1 as:

$$\Delta G^{crystal}(T) = -\frac{4\pi r^3}{3}\Delta G_V(T) + 4\pi r^2 \sigma_{C-G} \qquad (1)$$

where ΔG_V represents the free energy difference per volume between the glassy and the crystalline states, σ_{C-G} is the crystal-glass interfacial free energy, and r is the radius of the crystal nucleus.

During the devitrification $\Delta G_V(T) \approx \Delta H_m \left(1 - \frac{T}{T_m}\right)$ where ΔH_m is the melting enthalpy. The critical temperature Tc below which the nucleus survives within the liquid environment during the devitrification is provided by:

$$T_c = T_m \left(1 - \frac{2\sigma_{C-G}}{\Delta H_m r}\right) \qquad (2)$$

σ_{C-G}=0.11 J/m^2 is a reasonable approximation in the composition range of $\sim$40-78.1 %, σ_{C-G} is assumed to not vary substantially [97]. ΔH_m=8.20$\times$10^9 J/m^3 [98], and $r \approx$5 Å. We end up with a final value of $T_c \approx 0.94\ T_m$, whereas at t=8 ns when the devitrification starts $T \approx 0.87\ T_m$ which is below the predicted T_c. Therefore, we can conclude that the CNT is able to successfully predict a temperature range for CuZr MG devitrification confirmed by MD simulation. However, at this stage, there is no clear evidence indicating the exclusive influence of either temperature or compressive pressure effects on the observed devitrification process under the modeled ultrafast laser operating conditions.

D. Thermal *vs.* compressive effects

Additional classical MD simulations (*i.e.,* without relying on the TTM model) aiming at decorrelating the influence of the temperature and compressive wave on the devitrification process are presented in the following. The two additional simulations use as an input a subset of the original virtual sample described in Figure 4 with dimensions 8.13$\times$8.13$\times$8.13 nm^3, at t=0. The corresponding subsystem is subjected to stress (P_{xx}) and temperature cycles as close as those induced by the laser in the region where the transformation begins. While classical MD simulations do not reproduce the same exact dynamics as the TTM-MD approach, they may still offer valuable insights to help interpreting the phase transformation.

Two simulations are carried out without constraints on the sample volume and total energy. Firstly, the sample is heated from 300 K to 1000 K for 15 ps and then annealed at constant temperature for additional 85 ps before cooling down to 300 K over a period of 20 ns. This cycle exactly replicates the thermal conditions imposed by the laser in the region X$\sim$60 nm of the original sample (see Figure 4). Meanwhile, each component of the stress tensor is maintained at 0 GPa during the whole simulation process. In the second simulation, the same thermal cycle is followed, but P_{xx} is increased from 0 to 3 GPa during the first 15 ps, *i.e.*, during the heating process from 300 to 1000 K, before it is gradually reduced down to 0 GPa during the following next 85 ps. As in the other simulation, the sample is cooled down to 300 K between times t=100 ps and 20 ns. For further analysis, the local crystallography and Polyhedra evolution are monitored in the transformed zone along the entire process for both simulations. Results are depicted in Figure 10.

The left panel of Figure 10 illustrates the time evolution of <0,2,5,8> Polyhedra in the transformed zone of the sample subset for the two model simulations. The results demonstrate that the number of polyhedra broken during the initial stages of both simulations *i.e.*,

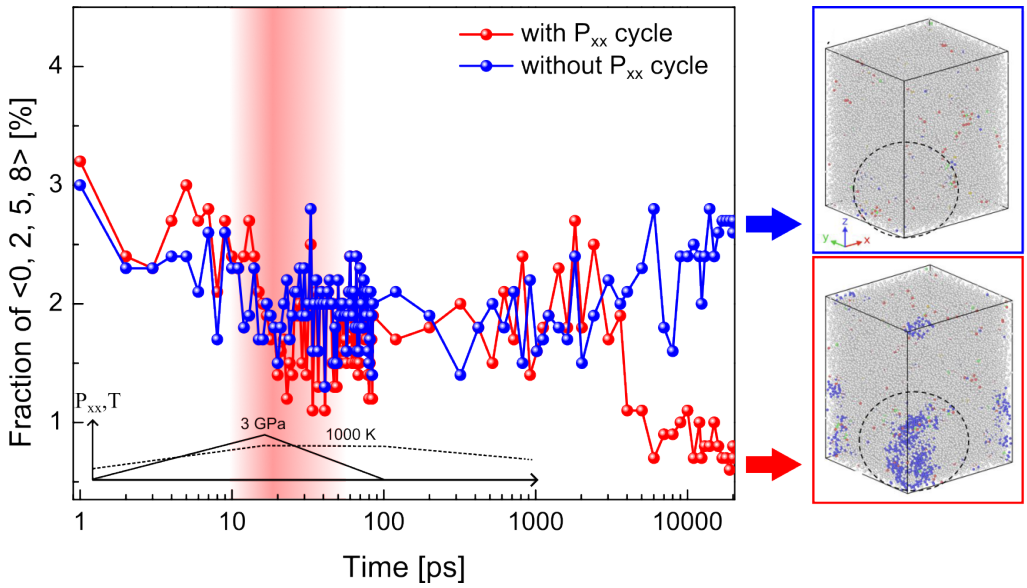

Figure 10. Polyhedra evolution and devitrification in the model classical MD simulations. Left panel: evolution of the fraction of <0,2,5,8> Polyhedra in the simulation (i) without stress (blue curve) and (ii) with a preliminary P_{xx}=0↗3↘0 GPa cycle, as computed in the transformed zone emphasized in the right panel (black-dashed lines). The red domain highlights a high-PT condition period during which the <0,2,5,8> fraction decreases in the simulation with stress cycle. Right panel: final atomic configurations for simulations with and without stress. In blue, we notice the formed crystalline BCC-like atoms (solid solution).

with or without the P_{xx} cycle, is of a similar magnitude. This finding further confirms the predominant role of temperature in driving this process. However, only the simulation with the P_{xx} cycle exhibits a phase transformation initiation similar to the one observed in the ultrafast laser simulation (Figure 10, right panel). Investigating more carefully the evolution of the polyhedra during the first 50 ps, one can see that the number of polyhedra decreases slightly more when the sample is subjected to a stress pulse concomitant to the heating process. Thus, the P_{xx} cycle acts as a hint upon the glass microstructure stability that helps the temperature at devitrifying the glass, in the operating conditions of the ultrafast laser simulated in the previous section. We believe that a similar process takes place in the laser simulation described in the previous section. Additional Gibbs-free energy calculations using the PM7 semi-empirical method that aim at characterizing the time-evolution of the transformation are presented in the Supplementary Information.

IV. APPLICATION TO PHONONIC THERMAL CONDUCTIVITY

In this last section, MD is employed to compute the phononic thermal conductivity (κ_a) in the partially devitrified glass. It has been demonstrated in recent studies that there is a possibility to improve κ_a of materials by using a femtosecond laser treatment on nanoparticles. This was mainly achieved in alumina and titanium dioxide as reported in the works of Ha *et al* [99, 100]. However, to our knowledge, no literature discussed the improvement of κ_a in amorphous compounds post-treated with an ultrafast laser. Furthermore, since amorphous CuZr alloys exhibit low κ_a values, the objective here is to examine the possible influence of crystal growth on κ_a.

Practically, κ_a is calculated in both the amorphous and composite structures employing the Green−Kubo method as implemented in LAMMPS [101–103]. The phonon thermal conductivity is given by the following equation:

$$\kappa_a = \frac{V}{3k_B T^2}\int_0^\infty \langle J(0)J(t)\rangle dt \qquad (3)$$

where V, k_B, T, J, and t describe volume, Boltzmann constant, temperature, instantaneous heat flux (with contributions from all components J_x, J_y, and J_z), and time respectively.

We use the initial (amorphous) and final (composite) configurations obtained from the laser-matter interaction simulation and probe the temperature sensitivity of the thermal conductivity. The thermal conductivity is computed in the 300-900 K temperature range. For this purpose, we first distribute the atom velocities and then

equilibrate the system during 20 ps within the NVE ensemble using a MD timestep of 1 fs. Then, we used a statistical method to compute the averaged value of the spontaneous heat autocorrelation flux $< J(0)J(t) >$ during 400 ps in the NVE ensemble. The result is illustrated in Figure 11.

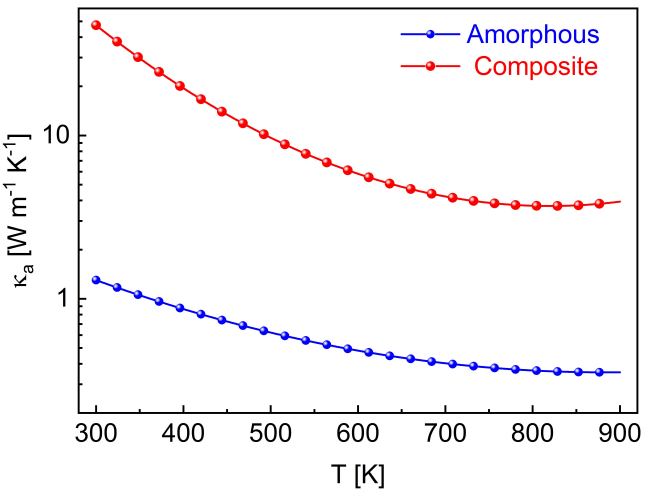

Figure 11. Phononic thermal conductivity of α-$Zr_{78.1}Cu_{21.9}$ in the amorphous phase and in the nanocomposite at various temperatures. Note the factor 36 between the two phases at T=300 K.

κ_a of both the nanocomposite and amorphous structures decreases when the temperature increases due to the rise of the phonon–phonon scattering rate [104]. κ_a of the amorphous structure also decreases significantly by 72 % (1.30 W $m^{-1}K^{-1}$ at 300 K to 0.36 W $m^{-1}K^{-1}$ at 900 K), whereas the composites one decreases by 92 % (47.33 W $m^{-1}K^{-1}$ at 300 K to 3.74 W $m^{-1}K^{-1}$ at 900 K). These results show that κ_a of the nanocomposite is ∼36 and ∼9 times larger than the one of the amorphous phase at T=300, 900 K, respectively. Therefore, the presence of nanocrystals within the amorphous α-$Zr_{78.1}Cu_{21.9}$ structure leads to the sharp increase of κ_a confirming that the local devitrification of amorphous structures is a promising approach for the creation of high-performance materials with exceptional properties at room temperature.

V. SUMMARY

In this study, the TTM-MD method is used to investigate the devitrification process induced by an ultrafast laser irradiating an α-$Cu_{21.9}Zr_{78.1}$ glass. Our results show that the ultrafast laser can be used to devitrify α-$Cu_{21.9}Zr_{78.1}$ leading to nucleation of BCC (solid solution) nanoprecicipitates localized at a few tens of nanometers below the sample surface. At the investigated fluency and pulse duration laser conditions, the main mechanism behind this phase transition is found to be the local atomic rearrangements (breaking of polyhedra) mostly induced by the heating and thermal relaxation cycles, assisted by the compressive wave generated by the laser. The temperature plays here a major role where the highest crystallization occurs at temperatures over T_g. Importantly, we observed that the crystalline nanoprecipitates are not transient but rather stable over time within the amorphous matrix. These results show that the ultrafast laser pulse technique can be used to generate very localized devitrification that promotes glass architecturation *i.e.*, from the laser focalisation at the sample surface to the in-depth controlled precipitation, suggesting that this method could be further employed in materials processing to create new nanoarchitectured systems, with enhanced material properties and efficiency, for modern industrial technologies.

DECLARATION OF COMPETING INTEREST

The authors declare that they have no known competing financial interests or personal relationships that could have appeared to influence the work reported in this paper.

ACKNOWLEDGMENTS

We gratefully acknowledge the ANR project MEGALIT (ANR-18-CE08) and the project FORMEL of the Pack Ambition Research program of the Auvergne Rhône-Alpes Region for supporting this work. Numerical computations were performed on the HPC resources from GENCI-TGCC and CINES, project gen7041.

SUPPLEMENTARY MATERIAL

Supplementary material associated with this article can be found, in the online version.

REFERENCES

[1] X. Li and Y. Guan, Theoretical fundamentals of short pulse laser–metal interaction: A review, Nanotechnology and Precision Engineering **3**, 105 (2020).

[2] L. Shen, P. Luo, Y. Hu, H. Bai, Y. Sun, B. Sun, Y. Liu, and W. Wang, Shear-band affected zone revealed by magnetic domains in a ferromagnetic metallic glass, Nature communications **9**, 1 (2018).

[3] H. Zhang, Y. Li, T. Xu, J. Wang, Z. Huo, P. Wan, and X. Sun, Amorphous co-doped mos 2 nanosheet coated metallic cos 2 nanocubes as an excellent electrocatalyst for hydrogen evolution, Journal of Materials Chemistry A **3**, 15020 (2015).

[4] M. Valant, U. Luin, M. Fanetti, A. Mavrič, K. Vyshniakova, Z. Siketić, and M. Kalin, Fully transparent nanocomposite coating with an amorphous alumina matrix and exceptional wear and scratch resistance, Advanced Functional Materials **26**, 4362 (2016).

[5] H. Guo, P. Yan, Y. Wang, J. Tan, Z. Zhang, M. Sui, and E. Ma, Tensile ductility and necking of metallic glass, Nature materials **6**, 735 (2007).

[6] Z.-J. Wang, M.-X. Li, J.-H. Yu, X.-B. Ge, Y.-H. Liu, and W.-H. Wang, Low-iridium-content irnita metallic glass films as intrinsically active catalysts for hydrogen evolution reaction, Advanced Materials **32**, 1906384 (2020).

[7] A. Schlegel, P. Wachter, K. Ackermann, M. Liard, and H.-J. Güntherodt, Optical properties of metallic glasses, Solid State Communications **31**, 373 (1979).

[8] B. T. Lester, T. Baxevanis, Y. Chemisky, and D. C. Lagoudas, Review and perspectives: shape memory alloy composite systems, Acta Mechanica **226**, 3907 (2015).

[9] T. Sahoo, B. Majumdar, V. Srinivas, M. Srinivas, T. Nath, and G. Agarwal, Improved magnetoimpedance and mechanical properties on nanocrystallization of amorphous fe68. 5si18. 5cu1nb3b9 ribbons, Journal of magnetism and magnetic materials **343**, 13 (2013).

[10] F. Qiu, P. Shen, T. Liu, and Q. Jiang, Enhanced ductility in a zr65cu15al10ni10 bulk metallic glass by nanocrystallization during compression, Materials & Design (1980-2015) **36**, 168 (2012).

[11] S. Yoon, G. Bae, Y. Xiong, S. Kumar, K. Kang, J.-J. Kim, and C. Lee, Strain-enhanced nanocrystallization of a cunitizr bulk metallic glass coating by a kinetic spraying process, Acta materialia **57**, 6191 (2009).

[12] J. Fornell, N. Van Steenberge, A. Varea, E. Rossinyol, E. Pellicer, S. Suriñach, M. Baró, and J. Sort, Enhanced mechanical properties and in vitro corrosion behavior of amorphous and devitrified ti40zr10cu38pd12 metallic glass, Journal of the Mechanical Behavior of Biomedical Materials **4**, 1709 (2011).

[13] P. Pawlik and H. Davies, Glass formability of fe–co–pr–dy–zr–b alloys and magnetic properties following devitrification, Scripta materialia **49**, 755 (2003).

[14] Y.-L. Gao, J. Shen, J.-F. Sun, G. Wang, D.-W. Xing, H.-Z. Xian, and B.-D. Zhou, Crystallization behavior of zralnicu bulk metallic glass with wide supercooled liquid region, Materials Letters **57**, 1894 (2003).

[15] D. Louzguine-Luzgin, Vitrification and devitrification processes in metallic glasses, Journal of alloys and compounds **586**, S2 (2014).

[16] M. Chen, T. Zhang, A. Inoue, A. Sakai, and T. Sakurai, Quasicrystals in a partially devitrified zr 65 al 7.5 ni 10 cu 12.5 ag 5 bulk metallic glass, Applied physics letters **75**, 1697 (1999).

[17] M. Scott, The crystallization kinetics of fe-ni based metallic glasses, Journal of Materials Science **13**, 291 (1978).

[18] Z. Lu and C. Liu, Glass formation criterion for various glass-forming systems, Physical Review Letters **91**, 115505 (2003).

[19] M. Bhat, V. Molinero, E. Soignard, V. Solomon, S. Sastry, J. Yarger, and C. Angell, Vitrification of a monatomic metallic liquid, Nature **448**, 787 (2007).

[20] A. M. Goryaeva, C. Fusco, M. Bugnet, and J. Amodeo, Influence of an amorphous surface layer on the mechanical properties of metallic nanoparticles under compression, Physical review materials **3**, 033606 (2019).

[21] M. Papanikolaou, K. Salonitis, M. Jolly, and M. Frank, Large-scale molecular dynamics simulations of homogeneous nucleation of pure aluminium, Metals **9**, 1217 (2019).

[22] J. J. Chu and C. A. Steeves, Thermal expansion and recrystallization of amorphous al and ti: A molecular dynamics study, Journal of non-crystalline solids **357**, 3765 (2011).

[23] A. Mahata, M. A. Zaeem, and M. I. Baskes, Understanding homogeneous nucleation in solidification of aluminum by molecular dynamics simulations, Modelling and Simulation in Materials Science and Engineering **26**, 025007 (2018).

[24] D. V. Louzguine-Luzgin and A. I. Bazlov, Crystallization of fcc and bcc liquid metals studied by molecular dynamics simulation, Metals **10**, 1532 (2020).

[25] Y. Zhang and S. Jiang, Atomistic mechanisms for temperature-induced crystallization of amorphous copper based on molecular dynamics simulation, Computational Materials Science **151**, 25 (2018).

[26] Q. Zhang, J. Wang, S. Tang, Y. Wang, J. Li, W. Zhou, and Z. Wang, Molecular dynamics investigation of the local structure in iron melts and its role in crystal nucleation during rapid solidification, Physical Chemistry Chemical Physics **21**, 4122 (2019).

[27] D. V. Louzguine-Luzgin, R. Belosludov, M. Saito, Y. Kawazoe, and A. Inoue, Glass-transition behavior of ni: Calculation, prediction, and experiment, Journal of Applied physics **104**, 123529 (2008).

[28] K. V. Manukyan, C. E. Shuck, M. J. Cherukara, S. Rouvimov, D. Y. Kovalev, A. Strachan, and A. S. Mukasyan, Exothermic self-sustained waves with amorphous nickel, The Journal of Physical Chemistry C **120**, 5827 (2016).

[29] L. Zhong, J. Wang, H. Sheng, Z. Zhang, and S. X. Mao, Formation of monatomic metallic glasses through ultrafast liquid quenching, Nature **512**, 177 (2014).

[30] M. Guerdane, F. Wendler, D. Danilov, H. Teichler, and B. Nestler, Crystal growth and melting in nizr alloy: Linking phase-field modeling to molecular dynamics simulations, Physical Review B **81**, 224108 (2010).

[31] S. Liu, Q. Cao, X. Mu, T. Xu, D. Wang, K. Ståhl, X. Wang, D. Zhang, C. Kübel, and J. Jiang, Tracing intermediate phases during crystallization in a ni–zr metallic glass, Acta Materialia **186**, 396 (2020).

[32] Q. Yang, S. Pang, and T. Zhang, Crystallization of amorphous ni-zr alloys during heating with molecular dynamics simulations, Journal of University of Science and Technology Beijing, Mineral, Metallurgy, Material **14**, 73 (2007).

[33] S. Kazanc, Molecular dynamics study of pressure effect on crystallization behaviour of amorphous cuni alloy during isothermal annealing, Physics Letters A **365**, 473 (2007).

[34] S. Rogachev, O. Politano, F. Baras, and A. Rogachev, Explosive crystallization in amorphous cuti thin films: a molecular dynamics study, Journal of Non-Crystalline Solids **505**, 202 (2019).

[35] A. Rogachev, S. Vadchenko, A. Aronin, S. Rouvimov, A. Nepapushev, I. Kovalev, F. Baras, O. Politano, S. Rogachev, and A. Mukasyan, Self-propagating waves of crystallization in metallic glasses, Applied Physics Letters **111**, 093105 (2017).

[36] M. Faruq, A. Villesuzanne, and G. Shao, Molecular-dynamics simulations of binary pd-si metal alloys: Glass formation, crystallisation and cluster properties, Journal of Non-Crystalline Solids **487**, 72 (2018).

[37] D. Nguyen-Trong, K. Pham-Huu, and P. Nguyen-Tri, Simulation on the factors affecting the crystallization process of feni alloy by molecular dynamics, ACS omega **4**, 14605 (2019).

[38] B.-y. Yu, Y.-c. Liang, Z.-a. Tian, R.-s. Liu, T.-h. Gao, Q. Xie, and Y.-f. Mo, Md simulation on crystallization mechanisms of rapidly supercooled fe-ni alloys, Journal of Crystal Growth **535**, 125533 (2020).

[39] Y. Sun, Z. Ye, F. Zhang, Z. J. Ding, C.-Z. Wang, M. J. Kramer, and K.-M. Ho, Investigation of partitionless growth of ε-al60sm11 phase in al-10 at% sm liquid, Modelling and Simulation in Materials Science and Engineering **26**, 015006 (2017).

[40] L. Zhao, G. Bokas, J. Perepezko, and I. Szlufarska, Nucleation kinetics in al-sm metallic glasses, Acta Materialia **142**, 1 (2018).

[41] S. Starikov, I. Gordeev, Y. Lysogorskiy, L. Kolotova, and S. Makarov, Optimized interatomic potential for study of structure and phase transitions in si-au and si-al systems, Computational Materials Science **184**, 109891 (2020).

[42] D. Nguyen Trong, V. Cao Long, and Ş. Ţălu, The structure and crystallizing process of niau alloy: a molecular dynamics simulation method, Journal of Composites Science **5**, 18 (2021).

[43] S. An, J. Li, Y. Li, S. Li, Q. Wang, and B. Liu, Two-step crystal growth mechanism during crystallization of an undercooled ni50al50 alloy, Scientific reports **6**, 1 (2016).

[44] S. Lesz and G. Dercz, Study on crystallization phenomenon and thermal stability of binary ni–nb amorphous alloy, Journal of Thermal Analysis and Calorimetry **126**, 19 (2016).

[45] M. Enayati, Crystallization behavior of ni-nb amorphous alloys, SCIENTIA IRANICA **9**, 157 (2002).

[46] M. Celtek, The effect of atomic concentration on the structural evolution of zr100-xcox alloys during rapid solidification process, Journal of Non-Crystalline Solids **513**, 84 (2019).

[47] J. Morris, M. Xu, Y. Ye, D. Sordelet, and M. Kramer, Theoretical and experimental studies of devitrification pathways in the zr2cu1- xpdx metallic glass system, Acta materialia **55**, 5901 (2007).

[48] A. Atila, M. Kbirou, S. Ouaskit, and A. Hasnaoui, On the presence of nanoscale heterogeneity in al70ni15co15 metallic glass under pressure, Journal of Non-Crystalline Solids **550**, 120381 (2020).

[49] R. Ryltsev, B. Klumov, N. Chtchelkatchev, and K. Y. Shunyaev, Computational crystallization of cu-zr-al glass-forming alloys, in The Tenth International Conference on Materials Technologies and Modelling MMT-2018 (2018) pp. 1122–1129.

[50] S. Lan, Z. Wu, X. Wei, J. Zhou, Z. Lu, J. Neuefeind, and X.-L. Wang, Structure origin of a transition of classic-to-avalanche nucleation in zr-cu-al bulk metallic glasses, Acta Materialia **149**, 108 (2018).

[51] K. Sahoo and R. Sahu, Glass transition and crystallization of al–ni–la based metallic glasses studied by temperature modulated dsc, Journal of non-crystalline solids **365**, 33 (2013).

[52] J. Tan, F. S. Pan, C. Li, J. Wang, and J. Eckert, Effect of fe on crystallization process of zr-co-al-(fe) bulk metallic glasses, in Materials Science Forum, Vol. 745 (Trans Tech Publ, 2013) pp. 734–739.

[53] X. Yang, C. Zhou, Q. Sun, L. Hu, J. C. Mauro, C. Wang, and Y. Yue, Anomalous crystallization as a signature of the fragile-to-strong transition in metallic glass-forming liquids, The Journal of Physical Chemistry B **118**, 10258 (2014).

[54] S. Mechler, N. Wanderka, and M.-P. Macht, Crystallization behavior of low temperature pre-annealed zr46. 8ti8. 2ni10cu7. 5be27. 5—bulk glass, Materials Science and Engineering: A **375**, 355 (2004).

[55] M. Wollgarten, S. Mechler, E. Davidov, N. Wanderka, and M.-P. Macht, Decomposition and crystallization of pd40cu30ni10p20 and zr46. 8ti8. 2cu7. 5ni10be27. 5 metallic glasses, Intermetallics **12**, 1251 (2004).

[56] U. Kühn, K. Eymann, N. Mattern, J. Eckert, A. Gebert, B. Bartusch, and L. Schultz, Limited quasicrystal formation in zr–ti–cu–ni–al bulk metallic glasses, Acta materialia **54**, 4685 (2006).

[57] C. Tang and P. Harrowell, Anomalously slow crystal growth of the glass-forming alloy cuzr, Nature materials **12**, 507 (2013).

[58] Y. Duan, J. Li, X. Zhang, T. Li, H. Arandiyan, Y. Jiang, and H. Li, Crystallization behavior of a confined cuzr metallic liquid film with a sandwich-like structure, Physical Chemistry Chemical Physics **21**, 13738 (2019).

[59] Y.-C. Hu and H. Tanaka, Physical origin of glass formation from multicomponent systems, Science advances **6**, eabd2928 (2020).

[60] T. Cullinan, I. Kalay, Y. E. Kalay, M. Kramer, and R. Napolitano, Kinetics and mechanisms of isothermal devitrification in amorphous cu50zr50, Metallurgical and Materials Transactions A **46**, 600 (2015).

[61] M. Prudent, D. Iabbaden, F. Bourquard, S. Reynaud, Y. Lefkir, A. Borroto, J.-F. Pierson, F. Garrelie, and J.-P. Colombier, High-density nanowells formation in ultrafast laser-irradiated thin film metallic glass, Nano-Micro Letters **14**, 1 (2022).

[62] J. Antonowicz, P. Zalden, K. Sokolowski-Tinten, K. Georgarakis, R. Minikayev, A. Pietnoczka, F. Bertram, M. Chaika, M. Chojnacki, P. Dłużewski, et al., Devitrification of thin film cu–zr metallic glass via ultrashort pulsed laser annealing, Journal of Alloys and Compounds **887**, 161437 (2021).

[63] C. Peng, L. Cheng, and M. Mansuripur, Experimental and theoretical investigations of laser-induced crystallization and amorphization in phase-change optical recording media, Journal of Applied Physics **82**, 4183 (1997).

[64] J. Cao, M. Lancry, F. Brisset, L. Mazerolles, R. Saint-Martin, and B. Poumellec, Femtosecond laser-induced crystallization in glasses: growth dynamics for oriented nanogratings and nanocrystallization, Crystal Growth & Design **19**, 2189 (2019).

[65] S. D. McAnany, K. J. Veenhuizen, A. M. Kiss, J. Thieme, D. A. Nolan, B. G. Aitken, V. Dierolf, and H. Jain, Evolution of glass structure during femtosecond laser assisted crystallization of labgeo5 in glass, Journal of Non-Crystalline Solids **551**, 120396 (2021).

[66] X. He, C. Fan, B. Poumellec, Q. Liu, H. Zeng, F. Brisset, G. Chen, X. Zhao, and M. Lancry, Size-controlled oriented crystallization in sio 2-based glasses by femtosecond laser irradiation, JOSA B **31**, 376 (2014).

[67] J.-M. Shieh, Z.-H. Chen, B.-T. Dai, Y.-C. Wang, A. Zaitsev, and C.-L. Pan, Near-infrared femtosecond laser-induced crystallization of amorphous silicon, Applied physics letters **85**, 1232 (2004).

[68] Y. Zhang, L. Liu, G. Zou, N. Chen, A. Wu, H. Bai, and Y. Zhou, Femtosecond laser-induced phase transformations in amorphous cu77ni6sn10p7 alloy, Journal of Applied Physics **117**, 023109 (2015).

[69] W. Zhou, F. Liu, N. Bai, Y. Wan, X. Lin, and J. Chen, Crystallization of amorphous ge2sb2te5 films induced by an ultraviolet laser, Applied surface science **285**, 97 (2013).

[70] G. Zhang, D. Gu, X. Jiang, Q. Chen, and F. Gan, Crystallization of amorphous ge2sb2te5 films induced by a single femtosecond laser pulse, Solid state communications **133**, 209 (2005).

[71] Y. Teng, J. Zhou, K. Sharafudeen, S. Zhou, K. Miura, and J. Qiu, Space-selective crystallization of glass induced by femtosecond laser irradiation, Journal of non-crystalline solids **383**, 91 (2014).

[72] S. Marinier and L. J. Lewis, Femtosecond laser ablation of cu x zr 1- x bulk metallic glasses: a molecular dynamics study, Physical Review B **92**, 184108 (2015).

[73] X. Wu, H. Yin, and Q. Li, Ablation and patterning of carbon nanotube film by femtosecond laser irradiation, Applied Sciences **9**, 3045 (2019).

[74] J. Krueger and W. Kautek, Femtosecond-pulse laser processing of metallic and semiconducting thin films, in Laser-Induced Thin Film Processing, Vol. 2403 (SPIE, 1995) pp. 436–447.

[75] `https://lammps.sandia.gov/doc/fix_ttm.html`.

[76] G. Norman, S. Starikov, V. Stegailov, I. Saitov, and P. Zhilyaev, Atomistic modeling of warm dense matter in the two-temperature state, Contributions to Plasma Physics **53**, 129 (2013).

[77] D. Duffy and A. Rutherford, Including the effects of electronic stopping and electron–ion interactions in radiation damage simulations, Journal of Physics: Condensed Matter **19**, 016207 (2006).

[78] V. Stegailov, S. Starikov, and G. Norman, Atomistic simulation of laser ablation of gold: The effect of electronic pressure, in AIP Conference Proceedings, Vol. 1426 (American Institute of Physics, 2012) pp. 905–908.

[79] A. Rutherford and D. Duffy, The effect of electron–ion interactions on radiation damage simulations, Journal of Physics: Condensed Matter **19**, 496201 (2007).

[80] A. P. Thompson, H. M. Aktulga, R. Berger, D. S. Bolintineanu, W. M. Brown, P. S. Crozier, P. J. in't Veld, A. Kohlmeyer, S. G. Moore, T. D. Nguyen, et al., Lammps-a flexible simulation tool for particle-based materials modeling at the atomic, meso, and continuum scales, Computer Physics Communications **271**, 108171 (2022).

[81] S. Plimpton, Fast parallel algorithms for short-range molecular dynamics, Journal of computational physics **117**, 1 (1995).

[82] M. Mendelev, Y. Sun, F. Zhang, C.-Z. Wang, and K.-M. Ho, Development of a semi-empirical potential suitable for molecular dynamics simulation of vitrification in cu-zr alloys, The Journal of Chemical Physics **151**, 214502 (2019).

[83] D. Iabbaden, J. Amodeo, C. Fusco, F. Garrelie, and J.-P. Colombier, Molecular dynamics simulation of structural evolution in crystalline and amorphous cuzr alloys upon ultrafast laser irradiation, Physical Review Materials **6**, 126001 (2022).

[84] D. J. Evans and B. L. Holian, The nose–hoover thermostat, The Journal of chemical physics **83**, 4069 (1985).

[85] A. Cao, Y. Cheng, and E. Ma, Structural processes that initiate shear localization in metallic glass, Acta Materialia **57**, 5146 (2009).

[86] C. Choy, K. Tong, H. Wong, and W. Leung, Thermal conductivity of amorphous alloys above room temperature, Journal of applied physics **70**, 4919 (1991).

[87] P. Garoche and J. Bigot, Comparison between amorphous and crystalline phases of copper-zirconium alloys by specific-heat measurements, Physical review B **28**, 6886 (1983).

[88] A. Stukowski, Structure identification methods for atomistic simulations of crystalline materials, Modelling and Simulation in Materials Science and Engineering **20**, 045021 (2012).

[89] P. M. Larsen, S. Schmidt, and J. Schiøtz, Robust structural identification via polyhedral template matching, Modelling and Simulation in Materials Science and Engineering **24**, 055007 (2016).

[90] A. Stukowski, Visualization and analysis of atomistic simulation data with ovito–the open visualization tool, Modelling and simulation in materials science and engineering **18**, 015012 (2009).

[91] S. Hao, C. Wang, M. Kramer, and K. Ho, Microscopic origin of slow dynamics at the good glass forming composition range in zr 1- x cu x metallic liquids, Journal of Applied Physics **107**, 053511 (2010).

[92] S. Zhou and R. Napolitano, Phase stability for the cu–zr system: first-principles, experiments and solution-based modeling, Acta Materialia **58**, 2186 (2010).

[93] M. Leocmach and H. Tanaka, Roles of icosahedral and crystal-like order in the hard spheres glass transition, Nature communications **3**, 974 (2012).

[94] M. Fanfoni and M. Tomellini, The johnson-mehl-avrami-kohnogorov model: a brief review, Il Nuovo Cimento D **20**, 1171 (1998).

[95] V. M. Fokin, E. D. Zanotto, N. S. Yuritsyn, and J. W. Schmelzer, Homogeneous crystal nucleation in silicate glasses: A 40 years perspective, Journal of Non-Crystalline Solids **352**, 2681 (2006).

[96] L. Cormier, Nucleation in glasses–new experimental findings and recent theories, Procedia Materials Science **7**, 60 (2014).

[97] D.-H. Kang, H. Zhang, H. Yoo, H. H. Lee, S. Lee, G. W. Lee, H. Lou, X. Wang, Q. Cao, D. Zhang, et al., Interfacial free energy controlling glass-forming ability of cu-zr alloys, Scientific reports **4**, 1 (2014).

[98] K. Yamaguchi, Y.-C. Song, T. Yoshida, and K. Itagaki, Thermodynamic investigation of the cu–zr system, Journal of alloys and compounds **452**, 73 (2008).

[99] J. Ha, Y. Seo, T.-Y. Choi, and D. Kim, Enhanced thermal conductivity of alumina nanoparticle suspensions

by femtosecond laser irradiation, International Journal of Heat and Mass Transfer **107**, 755 (2017).

[100] J. Ha, H. Jeon, T.-Y. Choi, and D. Kim, Enhancement of thermal conductivity of titanium dioxide nanoparticle suspensions by femtosecond laser irradiation, International Journal of Heat and Mass Transfer **133**, 662 (2019).

[101] D. Surblys, H. Matsubara, G. Kikugawa, and T. Ohara, Application of atomic stress to compute heat flux via molecular dynamics for systems with many-body interactions, Physical Review E **99**, 051301 (2019).

[102] P. Boone, H. Babaei, and C. E. Wilmer, Heat flux for many-body interactions: corrections to lammps, Journal of chemical theory and computation **15**, 5579 (2019).

[103] D. Surblys, H. Matsubara, G. Kikugawa, and T. Ohara, Methodology and meaning of computing heat flux via atomic stress in systems with constraint dynamics, Journal of Applied Physics **130**, 215104 (2021).

[104] J. M. Ziman, Electrons and phonons: the theory of transport pheno (Oxford university press, 2001).